JOURNAL OF THE AMERICAN HELICOPTER SOCIETY **70**, 042007 (2025)

Redundant Control Allocation Strategies for the RACER Compound Rotorcraft Configuration

Umberto Saetti*
Assistant Professor
Department of Aerospace Engineering, University of Maryland, College Park, MD

This article presents the development, implementation, and evaluation of dynamic inversion (DI) flight control laws for compound rotorcraft with auxiliary propulsion systems, with application to a configuration representative of the Airbus Rapid And Cost-Efficient Rotorcraft (RACER). The RACER features a single main rotor, a boxed wing, and two lateral pusher propellers that provide both torque balancing and thrust compounding. The DI control laws are structured using a multiloop architecture and incorporate redundant control allocation to the pusher propellers via a pseudo-inverse (PI) strategy. A primary objective is to investigate control allocation approaches that minimize pitch attitude excursions during acceleration and deceleration maneuvers. A generic multirotor/wing simulation model is adapted to model the flight dynamics of the RACER configuration. The model is trimmed and linearized at discrete speeds from hover to cruise, and control reallocation is used to enable trimming at arbitrary pitch attitudes. Model-order reduction techniques are applied to obtain reduced-order models suitable for control synthesis. Both a baseline DI controller and a PI variant are implemented and tested in closed-loop simulations using the full-order nonlinear model. Three representative maneuvers are considered: (i) a hover-to-cruise transition, (ii) a combined transition, climb, and coordinated turn, and (iii) a cruise-to-hover reverse transition. The PI-based control law reduces pitch attitude variation by reallocating control effort to the auxiliary propulsion system, while achieving comparable tracking accuracy, as well as similar performance and handling-quality metrics relative to the baseline controller.

Introduction

Future vertical lift (FVL) and electric vertical take-off and landing (eVTOL) vehicles developed for urban air mobility (UAM) frequently adopt multirotor architectures and rigid rotor systems, resulting in strong aerodynamic interactions and coupling effects. These characteristics introduce significant challenges for flight dynamics modeling, simulation, and control system development. Representative FVL concepts include winged single main rotor, lift-offset coaxial, and tiltrotor platforms (Refs. 1–4). Likewise, recent efforts to classify eVTOL architectures have identified two broad categories: rotary-wing cruise and fixed-wing cruise configurations (Refs. 5, 6). The former includes rotary-wing and lift-fan designs, while the latter encompasses lift+cruise, tilt-wing/tiltrotor, and tailsitter vehicles. These hybrid configurations often feature operational modes with significantly different aerodynamic characteristics, necessitating careful treatment of control system design across transitions between hover and forward flight.

A representative configuration that incorporates elements from both rotary- and fixed-wing systems is the Airbus RACER (Rapid and Cost-Efficient Rotorcraft), a compound rotorcraft demonstrator developed under the European Union's Clean Sky 2 initiative. The RACER design integrates lift and thrust compounding, with lift provided by a single main rotor and a joined box-wing, and longitudinal thrust generated by two lateral pusher propellers. These propellers also contribute to yaw control and torque balancing (Ref. 7). The empennage includes a vertical fin and horizontal stabilizers that support directional and pitch stability and are subject to wake interactions from both the main rotor and the pusher propellers. The RACER configuration introduces multiple coupled aerodynamic and control considerations, making it a relevant testbed for evaluating modeling and control strategies for advanced compound rotorcraft.

Several recent studies have explored the aerodynamic and flight mechanics characteristics of RACER using high-fidelity computational fluid dynamics and coupled flight dynamics simulations. These include assessments of rotor wake interactions with the fuselage and tail surfaces, evaluation of control surface effectiveness in crosswind hover, and analyses of inflow distortion at the pusher propellers due to their location in the rotor downwash (Refs. 7–10). Further investigations have addressed rotor-on-tail interference (Ref. 11), vertical fin aerodynamic design (Ref. 12), and the integrated aeroacoustic footprint of the configuration across operating conditions (Ref. 10).

These aerodynamic phenomena directly affect handling qualities and underscore the importance of robust control strategies. Key challenges specific to RACER and similar hybrid configurations include (i) transition between hover and high-speed flight regimes, during which the aerodynamic contribution of the box-wing becomes significant; (ii)

---

*Corresponding author; email: saetti@umd.edu

Manuscript received May 2025; accepted August 2025.

DOI: 10.4050/JAHS.70.042007

significant shifts in stability and response characteristics across flight conditions (Ref. 7); (iii) nonlinear and asymmetric rotor–wing–propeller interactions that vary with advance ratio and wind conditions (Refs. 8, 9); (iv) the need for coordinated use of multiple effectors, including auxiliary propulsion, for both torque and trajectory control (Ref. 10); and (v) increased sensitivity to atmospheric disturbances, requiring model-based control augmentation for gust rejection and handling-quality assurance.

To address these challenges, control system architectures must be both flexible and robust, capable of maintaining stability and tracking performance across flight regimes while minimizing pilot workload. Prior research on model-following strategies for compound rotorcraft has employed explicit model following (EMF), linear and nonlinear dynamic inversion, and hybrid approaches (Refs. 13–19). Among these, Refs. 16–18 focused on evaluating handling qualities.

Model-following control architectures, such as dynamic inversion (DI) and EMF, are particularly well-suited for gust disturbance rejection. Their two-degree-of-freedom structure, comprising separate feed-forward and feedback paths, enables the tuning of rotorcraft responses to gusts independently of the responses to outer-loop guidance and navigation commands. In contrast, classical one-degree-of-freedom control approaches do not offer such decoupling, making independent tuning of these responses more challenging. Both methods rely on model inversion to cancel plant dynamics and track a desired reference model. EMF employs a simplified linear inversion and requires gain scheduling. DI consolidates scheduling into the plant model, reducing controller complexity at the expense of requiring accurate, flight-condition-dependent plant characterization. Previous work on DI for high-speed compound rotorcraft has applied hybrid control strategies combining DI outer loops with EMF-based inner loops (Refs. 16, 17), often demonstrated through quasi-linear parameter varying models (Ref. 20). However, no published study has demonstrated a pure DI control law using active allocation to auxiliary propulsion systems that simultaneously provide torque balancing and thrust compounding, as is the case with RACER.

While published research on the RACER platform has primarily focused on conceptual design, interactional aerodynamics, and aeroacoustics, this study explores the use of active control allocation strategies for both trim and maneuvering flight by leveraging the decoupling of longitudinal thrust generation from pitch attitude changes via auxiliary propulsion systems. Specifically, the objectives of this investigation are twofold: (i) to formulate a control allocation strategy that enables trimmed flight at arbitrary pitch attitudes by redirecting control effort to the auxiliary propulsion units; and (ii) to evaluate the extent to which active control allocation can minimize pitch attitude excursions during acceleration and deceleration maneuvers.

The paper begins with an overview of the simulation model and its adaptation to a configuration representative of the Airbus RACER. This is followed by a detailed mathematical description of the linearization, trim, and model-order reduction algorithms. DI control laws are then developed using a multiloop architecture combined with a proportional-integral (PI) redundant control allocation strategy. These laws are parameterized by flight speed to enable automatic transitions between hover and cruise. The control framework is demonstrated âŁ”both with and without control reallocation—through simulations of transitions to and from hover. Final remarks summarize the key findings and outline directions for future research.

Simulation Models

Overview

Simulation models are based on an in-house MATLAB®/Simulink generic multirotor/wing flight dynamics and control code with the following characteristics:

(1) The aircraft fuselage is modeled as a rigid body. Fuselage aerodynamic forces are calculated based on equivalent flat-plate frontal, lateral, and vertical areas (Ref. 21).

(2) The user can specify any number of rotors and/or wings at arbitrary (and time-varying) orientations on the aircraft body.

(3) Accuracy of the rotor aeromechanics is selectable, with modeling methods being as simple as static inflow and no blade flapping, or as complex as dynamic inflow (Ref. 22) and flexible blades based on finite element methods. Rotor aerodynamics can also account for rotor-on-rotor interactions (Refs. 23–26).

(4) Wings' accuracy level is also selectable. The most complex model consists of lifting-line theory. Rotor-on-wing aerodynamics interactions are calculated based on the circulation at each wing element/panel using Biot–Savart and Heyson (Ref. 27).

(5) The model is implemented in MATLAB® to ease the design and testing of flight control laws.

(6) The model is integrated with a baseline control law based on DI (Refs. 28–30), featuring inner-attitude and outer-velocity control loops. Collective pitch control is implemented as part of the outer loop architecture.

It is worth noting that this code was validated against flight-test data for various other configurations in prior studies, including H-60, XV-15, and small-scale unmanned aerial systems (Refs. 31, 32).

A simulation model is developed for a configuration reminiscent of the Airbus RACER, featuring a single main rotor, two pusher propellers used for torque/thrust compounding, a boxed wing, and an "H" tail with trim tabs. This configuration will be referred to as "RACER." The geometry of the RACER configuration is shown in trimmed flight at hover in Fig. 1. Note that, for illustration purposes, the geometry of the ROtor-Body-INteraction (ROBIN) fuselage (Refs. 33, 34) is used. This is because it was not possible to reproduce the RACER fuselage based on publicly available data. The general characteristics of the RACER configuration are reported in Table 1. The RACER properties are estimated from publicly available pictures/drawings found online or scaled from rotorcraft for which the properties are known, for example, UH-60 and XV-15 from Refs. 35 and 36.

Nonlinear dynamics

The rotorcraft flight dynamics are formulated as a nonlinear time-periodic system:

$$\dot{\boldsymbol{x}} = \boldsymbol{f}(\boldsymbol{x}, \boldsymbol{u}, t) \tag{1a}$$

$$\boldsymbol{y} = \boldsymbol{g}(\boldsymbol{x}, \boldsymbol{u}, t) \tag{1b}$$

where $\boldsymbol{x} \in \mathbb{R}^n$ is the state vector, $\boldsymbol{u} \in \mathbb{R}^m$ is the control input vector, $\boldsymbol{y} \in \mathbb{R}^l$ is the output vector, and t is the dimensional time in seconds. It is convenient to note that dimensional time can be related to the azimuth angle ψ of a reference blade, also known as nondimensional time, via the following relation: $\psi = \Omega t$, where Ω is the angular speed, in rad/s, of the slowest rotor. It follows that the fundamental period of the system is $T = (2\pi)/\Omega$ seconds, which corresponds to 2π radians or one revolution of the slowest rotor. The nonlinear functions $\boldsymbol{f}$ and $\boldsymbol{g}$ are T-periodic in time such that

$$\boldsymbol{f}(\boldsymbol{x}, \boldsymbol{u}, t) = \boldsymbol{f}(\boldsymbol{x}, \boldsymbol{u}, t + T) \tag{2a}$$

$$\boldsymbol{g}(\boldsymbol{x}, \boldsymbol{u}, t) = \boldsymbol{g}(\boldsymbol{x}, \boldsymbol{u}, t + T) \tag{2b}$$

The state vector is

$$\boldsymbol{x}^T = \left[\boldsymbol{x}_{\mathrm{RB}}^T\ \boldsymbol{x}_{\mathrm{R}_1}^T\ \cdots\ \boldsymbol{x}_{\mathrm{R}_N}^T\right] \tag{3}$$

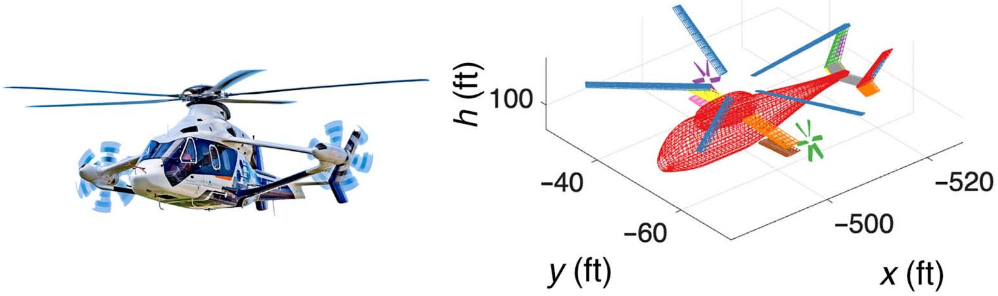

(a) Airbus RACER[1] **(b)** Simulation model

Fig. 1. Compound rotorcraft geometry at hover. (a) Airbus RACER ([1]https://www.clean-aviation.eu/news-events/a-very-successful-flight-test-of-the-racer-helicopter-demonstrator-in-marignane). (b) Simulation model.

where $\boldsymbol{x}_{\mathrm{RB}}$ are the rigid-body states and $\boldsymbol{x}_{\mathrm{R}_i}$ are the states of the ith of N rotors. The rigid-body state vector is common to all aircraft and is given by

$$\boldsymbol{x}_{\mathrm{RB}}^T = [u \; v \; w \; p \; q \; r \; \phi \; \theta \; \psi \; x \; y \; z] \tag{4}$$

where $u, \; v, \; w$ are the longitudinal, lateral, and vertical velocities in the body-fixed frame; $p, \; q, \; r$ are the roll, pitch, and yaw rates; $\phi, \; \theta, \; \psi$ are the Euler angles; and $x, \; y, \; z$ are the positions in the North-East-Down frame.

The general form of the ith rotor state vector is

$$\boldsymbol{x}_{\mathrm{R}_i}^T = \left[\boldsymbol{\beta}_{\mathrm{M}}^T \; \dot{\boldsymbol{\beta}}_{\mathrm{M}}^T \; \boldsymbol{\lambda}^T \; \Omega \; \psi_{\mathrm{R}}\right] \tag{5}$$

where $\boldsymbol{\beta}_{\mathrm{M}}$ are the flapping angles in multi-blade coordinated, $\boldsymbol{\lambda}^T = [\lambda_0 \; \lambda_{1c} \; \lambda_{1s}]$ is a vector containing the dynamic inflow components, Ω is the rotor angular speed, and ψ_{R} is the azimuth angle of a reference blade.

The pilot stick input vector is

$$\boldsymbol{u}^T = \left[\delta_{\mathrm{lat}} \; \delta_{\mathrm{lon}} \; \delta_{\mathrm{col}} \; \delta_{\mathrm{ped}} \; \delta_{\mathrm{aux}}\right] \tag{6}$$

where δ_{lat} is the lateral and longitudinal stick position, δ_{lat} and δ_{lon} are the longitudinal stick position, δ_{col} is the collective stick position, δ_{ped} is the pedal position, and δ_{aux} is an auxiliary input that controls the rotor/wing tilt angle.

The pilot inputs are converted to actuator inputs via mixing matrices scheduled with aircraft's absolute speed. The control effector inputs are

$$\boldsymbol{u}_{\mathrm{C}}^T = \left[\boldsymbol{u}_{\mathrm{R}}^T \; \boldsymbol{u}_{\mathrm{W}}^T\right] \tag{7}$$

where $\boldsymbol{u}_{\mathrm{R}}$ are the rotor actuator inputs and $\boldsymbol{u}_{\mathrm{W}}$ are the wing actuator inputs. The actuator inputs for the ith rotor are

$$\boldsymbol{u}_{\mathrm{R}_i}^T = [\theta_0 \; \theta_{1c} \; \theta_{1s} \; \Omega_{\mathrm{cmd}} \; \beta_{\mathrm{R}}] \tag{8}$$

where $\theta_0 \; \theta_{1s} \; \theta_{1c}$ are the collective, longitudinal cyclic, and lateral cyclic swashplate inputs; Ω_{cmd} is the commanded rotor speed; and β_{R} is the rotor tilt angle.

It is worth noting that the pusher propellers are assumed to be pitch-only controlled and their angular speed to be constant. The main rotor speed is also prescribed with speed and it drops from 100 to 85% of its hover value between 120 and 160 kt. The actuator inputs for the ith wing are

$$\boldsymbol{u}_{\mathrm{W}_i}^T = \left[\beta_{\mathrm{W}} \; \delta_{\mathrm{TE}} \; \cdots \; \delta_{\mathrm{TE}_N}\right] \tag{9}$$

where β_{W_i} is the wing tilt angle and δ_{TE_j} is the deflection of the jth trailing edge.

Trim, linearization, and model-order reduction

Linearized, time-invariant models are obtained by trimming the rotorcraft flight dynamics at a desired flight condition via the periodic trim algorithm of Refs. 37 and 29. Subsequently, the rotorcraft flight dynamics are linearized about each trim point via perturbation methods by only retaining the averaged (or zeroth) dynamics. To eliminate the need to measure or estimate states associated with the higher order dynamics, where the higher order dynamics include rotor and higher harmonic dynamics, it is desirable to reduce the order of the linearized dynamics. This is a necessary step to make linearized models tractable for practical control design purposes. This is achieved through residualization, a portion of singular perturbation theory that pertains to Linear Time Invariant systems (Ref. 38). Application of residualization to the rotorcraft flight dynamics can be found in several published research studies, for example, Refs. 28, 29, and 39–43.

Flight Control Design

General architecture

The flight control architecture chosen for this study is nonlinear dynamic inversion (NDI). Application of NDI control laws to rotorcraft can be found in Refs. 16, 25, 29, 30, 39, 41, 42, and 44–50. A key aspect of DI is the reliance on model inversion to cancel the plant dynamics and track a desired reference model. One convenient feature of NDI is that it inverts the plant model within its feedback linearization loop. Compared to other conventional model-following control strategies, such as EMF, this approach reduces the explicit need for gain scheduling of the outer-loop control laws. However, the plant model used for feedback linearization still requires scheduling with the flight condition, as variations in aircraft dynamics must be accounted for. Additionally, the feedback gains may need to be scheduled in cases where consistent disturbance rejection (measured in disturbance rejection bandwidth) and robustness performance (measured in broken-loop crossover frequency) must be maintained across the flight envelope. A generic DI controller as applied to a linear system is shown in Fig. 2. The key components include a command model (also referred to as a command filter or reference model) that specifies the desired response to pilot commands, a feedback compensation loop that minimizes tracking error, and an inner feedback loop that performs model inversion (i.e., the feedback linearization loop).

A multiloop NDI control law based on Refs. 16, 25, 28, 29, and 44 is designed to enable automatic flight in low-speed flight, cruise flight, and transition between the two. The schematic of the closed-loop

Table 1. General characteristics of the RACER model. Properties are estimated from publicly available pictures/drawings or scaled from rotorcraft for which the properties are known, for example, UH-60 and XV-15 (Refs. 35, 36).

Parameter	Value	Units
Mass and inertia		
Gross weight, W	11905	lb
Roll-axis moment of inertia, I_{xx}	14000	sl-ft^2
Pitch-axis moment of inertia, I_{yy}	23500	sl-ft^2
Yaw-axis moment of inertia, I_{zz}	32500	sl-ft^2
Roll/yaw-axes product of inertia, I_{xz}	900	sl-ft^2
CG fuselage station	15.6	ft
CG butt line	0	ft
CG water line	4.32	ft
Fuselage		
Frontal drag area	26.38	ft^2
Sideward drag area	198.41	ft^2
Vertical drag area	169.34	ft^2
Fuselage station (center of pressure)	15.6	ft
Butt line (center of pressure)	0	ft
Water line (center of pressure)	3.32	ft
Main rotor		
Number of blades	5	–
Radius	23	ft
Mean blade chord	1.33	ft
Angular speed (hover)	23.04	rad/s
Angular speed (cruise)	19.58	rad/s
Blade twist	−12	deg
Blade weight	167.6	lb
Blade first mass moment	56.5	sl-ft^2
Blade second mass moment	846.6	sl-ft^2
Fuselage station	15.6	ft
Butt line	0	ft
Water line	10.33	ft
Propellers		
Number of blades	6	–
Radius	3.51	ft
Mean blade chord	0.66	ft
Angular speed	135	rad/s
Blade twist	−40	deg
Fuselage station	20.24	ft
Butt line	±12.16	ft
Water line	4.32	ft
Wings		
Span	8.52	ft
Mean chord	2.93	ft
Cant angle	±12.5	deg
Sweep	±10	deg
Fuselage station (aerodynamic center)	{15.79, 18.96}	ft
Butt line (aerodynamic center)	±7.43	ft
Water line (aerodynamic center)	{1.94, 5.3}	ft
Horizontal/vertical stabilizers		
Span	{7.63, 7.39}	ft
Mean chord	{2.66, 2.63}	ft
Sweep	{20, 30}	deg
Fuselage station (aerodynamic center)	{36.32, 38.19}	ft
Butt line (aerodynamic center)	{0, ±4.1}	ft
Water line (aerodynamic center)	{4.06, 6.45}	ft

rotorcraft dynamics is shown in Fig. 3. The outer loop controller, shown in Fig. 5, tracks longitudinal, lateral, and vertical ground velocities commands in the heading frame and calculates the desired pitch and roll attitudes for the inner loop to track, in addition to the collective control input setting. The desired response type for the outer loop is translational rate command. The inner loop, shown in Fig. 4, achieves stability, disturbance rejection, and desired response characteristics about the roll, pitch, yaw, and heave axes. When coupled with the outer loop, an attitude command/attitude hold (ACAH) response is used for the roll and pitch axes, whereas Rate Command / Direction Hold (RCDH) is used for the yaw axis.

Inner-attitude loop

The modified state vector used for the inner-attitude loop design is

$$\boldsymbol{x}^T = [p\ q\ r\ \phi\ \theta] \tag{10}$$

The system and control matrices of the corresponding modified system (i.e., $\boldsymbol{A}$ and $\boldsymbol{B}$) are obtained by truncating the rows and columns corresponding to the body-axes linear velocity states. Note that the stability and control derivatives are a function of the total speed $V = \sqrt{u^2 + v^2 + w^2}$. The controlled variables are

$$\boldsymbol{y}^T = [\phi\ \theta\ r] \tag{11}$$

The output matrix that relates the state vector to the output vector:

$$\boldsymbol{C}^T = \left[\boldsymbol{C}_1^T\ \boldsymbol{C}_2^T\right] \tag{12}$$

where

$$\boldsymbol{C}_1 = \begin{bmatrix} 0 & 0 & 0 & 1 & 0 \\ 0 & 0 & 0 & 0 & 1 \end{bmatrix} \tag{13a}$$

$$\boldsymbol{C}_2 = [0\ \ 0\ \ 1\ \ 0\ \ 0] \tag{13b}$$

In the equation above, $\boldsymbol{C}_1$ corresponds to the roll and pitch attitudes, whereas $\boldsymbol{C}_2$ corresponds to the yaw rate. This partitioning is due to the fact that the output equations for ϕ and θ must be differentiated twice to have the control inputs appear explicitly in the output equation, while the same procedure requires being performed once for the yaw rate r:

$$\begin{bmatrix} \ddot{\phi} \\ \ddot{\theta} \\ \dot{r} \end{bmatrix} = \begin{bmatrix} \boldsymbol{C}_1\boldsymbol{A}^2\boldsymbol{x} + \boldsymbol{C}_1\boldsymbol{A}\boldsymbol{B}\boldsymbol{u} \\ \boldsymbol{C}_2\boldsymbol{A}\boldsymbol{x} + \boldsymbol{C}_2\hat{\boldsymbol{B}}\boldsymbol{u} \end{bmatrix} \tag{14}$$

The objective of the DI control law is that the output $\boldsymbol{y}$ tracks a reference trajectory $\boldsymbol{y}_{\text{cmd}}(t)$ given by

$$\boldsymbol{y}_{\text{cmd}}^T = [\phi_{\text{cmd}}\ \theta_{\text{cmd}}\ r_{\text{cmd}}] \tag{15}$$

with desired response characteristics. For this reason, the reference trajectory is fed through first- or second-order command models which dictate the desired response of the system. More specifically, ϕ_{cmd} and θ_{cmd} are fed through a second-order system, whereas r_{cmd} is fed through a first-order system. The command models are also used to extract the first and second derivatives of the filtered reference trajectory for use in the PI and proportional-integral-derivative (PID) compensators. The command models are also used to extract the first and second derivatives of the filtered reference trajectory for use in the PI and PID compensators described below. The command models are of the following form:

$$G_{\text{ideal}}^{(1)}(s) = \frac{1}{\tau s + 1} \tag{16a}$$

$$G_{\text{ideal}}^{(2)}(s) = \frac{\omega_n^2}{s^2 + 2\omega_n\zeta + \omega_n^2} \tag{16b}$$

where τ is the first-order command model time constant, which is the inverse of the command model break frequency (i.e., $\tau = 1/\omega_n$). Additionally, ω_n and ζ are, respectively, the natural frequency and damping ratio of the second-order command model. PI and PID compensation are used to reject external disturbances and to compensate for discrepancies

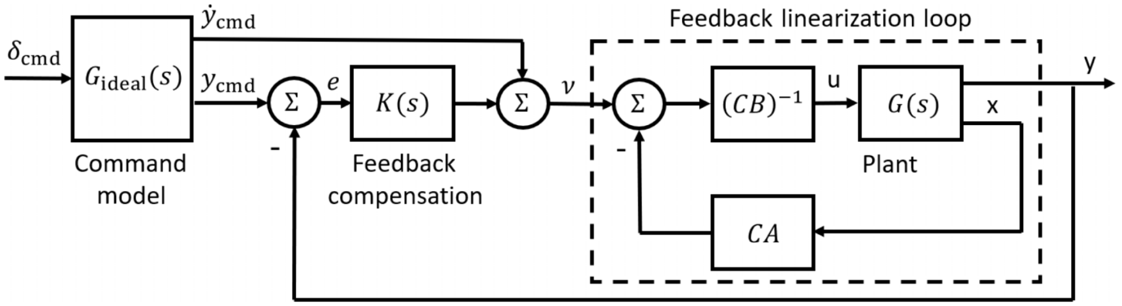

Fig. 2. DI controller as applied to a linear system.

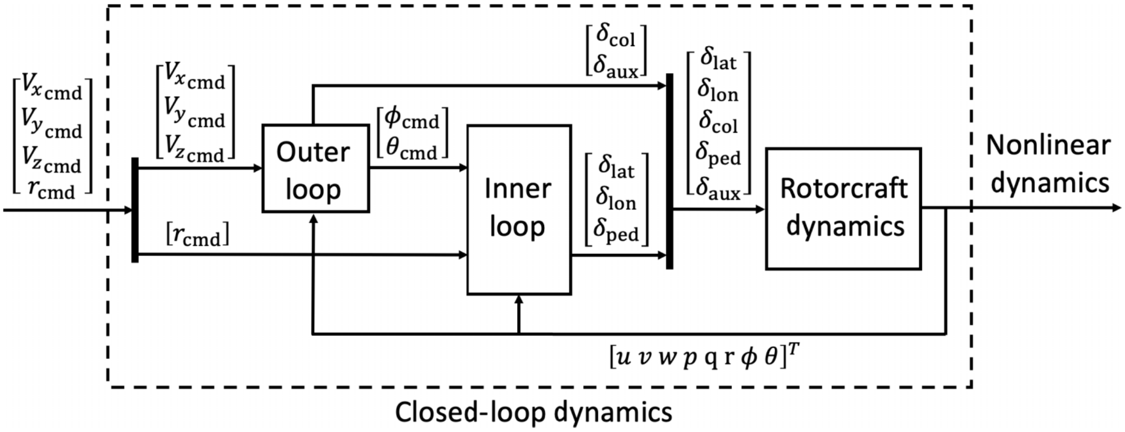

Fig. 3. Schematic of the closed-loop rotorcraft dynamics.

between the approximate model used in this derivation and the actual bare-airframe dynamics of the aircraft. The resulting DI control law is found by solving for the control vector in Eq. (14), leading to

$$\boldsymbol{u} = \begin{bmatrix} \boldsymbol{C}_1\boldsymbol{A}\boldsymbol{B} \\ \boldsymbol{C}_2\boldsymbol{B} \end{bmatrix}^{-1} \left(\boldsymbol{\nu} - \begin{bmatrix} \boldsymbol{C}_1\boldsymbol{A}^2 \\ \boldsymbol{C}_2\boldsymbol{A} \end{bmatrix} \boldsymbol{x} \right) \tag{17}$$

where $\boldsymbol{\nu}$ is the pseudo-command vector and $\boldsymbol{e}$ is the error as defined in Eqs. (18) and (19), respectively.

$$\begin{bmatrix} \nu_\phi \\ \nu_\theta \\ \nu_r \end{bmatrix} = \begin{bmatrix} \ddot{\phi}_{\text{cmd}} \\ \ddot{\theta}_{\text{cmd}} \\ \dot{r}_{\text{cmd}} \end{bmatrix} + \boldsymbol{K}_P \begin{bmatrix} e_\phi \\ e_\theta \\ e_r \end{bmatrix} + \boldsymbol{K}_D \begin{bmatrix} \dot{e}_\phi \\ \dot{e}_\theta \\ 0 \end{bmatrix} + \boldsymbol{K}_I \begin{bmatrix} \int e_\phi dt \\ \int e_\theta dt \\ \int e_r dt \end{bmatrix} \tag{18}$$

$$\boldsymbol{e} = \boldsymbol{y}_{\text{cmd}} - \boldsymbol{y}; \tag{19}$$

The diagonal matrices $\boldsymbol{K}_P \in \mathbb{R}^{3\times3}$, $\boldsymbol{K}_I \in \mathbb{R}^{3\times3}$, and $\boldsymbol{K}_D \in \mathbb{R}^{3\times3}$ identify the PI and derivative gain matrices, respectively. The command model parameters adopted are shown in Table 2. Note that the coefficient matrices $(\boldsymbol{C}_1\boldsymbol{A}\boldsymbol{B})^{-1}$, $\boldsymbol{C}_1\boldsymbol{A}^2$, $(\boldsymbol{C}_2\boldsymbol{B})^{-1}$, and $\boldsymbol{C}_2\boldsymbol{A}$ are functions of the total speed of the aircraft V. For this reason, from a practical standpoint, these matrices are computed offline at incremental longitudinal speeds from hover to the maximum speed of the aircraft at 20 kt intervals and stored. When the linearized DI controller is implemented on the nonlinear aircraft dynamics, the coefficient matrices $(\boldsymbol{C}_1\hat{\boldsymbol{A}}\hat{\boldsymbol{B}})^{-1}$, $\boldsymbol{C}_1\boldsymbol{A}^2$, $(\boldsymbol{C}_2\boldsymbol{B})^{-1}$, and $\boldsymbol{C}_2\boldsymbol{A}$ are computed at each time step via interpolation based on the current airspeed $V(t)$ and on the lookup tables stored offline. It is important to note that what is implemented on the nonlinear aircraft dynamics is linearized DI. However, because the coefficient matrices are scheduled with the longitudinal speed, and scheduling effectively introduces a nonlinear relation between the aircraft states and the feedback control input, the controller implemented is effectively NDI (Ref. 28). The inner loop schematics are shown in Fig. 4.

Table 2. Inner loop command models parameters.

Command	ω_n(rad/s)	ζ
Roll attitude	4.5	0.7
Pitch attitude	4.0	0.7
Yaw rate	2	–

Outer-velocity loop

The objective of the outer-velocity loop is to track longitudinal and lateral velocities in the heading frame, such that the reference trajectory is given by

$$\boldsymbol{y}_{\text{cmd}}^T = \left[V_{x_{\text{cmd}}}\ V_{y_{\text{cmd}}}\ V_{z_{\text{cmd}}}\right] \tag{20}$$

The heading frame is a vehicle-carried frame where the x-axis is aligned with the current aircraft heading, the z-axis is positive up in the inertial frame, and the y-axis points to the right, forming a left-handed orthogonal coordinate system. The following equation shows the rotation from the body to the heading frame:

$$\boldsymbol{T}_{B\to h} = \begin{bmatrix} \cos\theta & \sin\phi\sin\theta & \cos\phi\sin\theta \\ 0 & \cos\phi & -\sin\phi \\ \sin\theta & -\sin\phi\cos\theta & -\cos\phi\cos\theta \end{bmatrix} \tag{21}$$

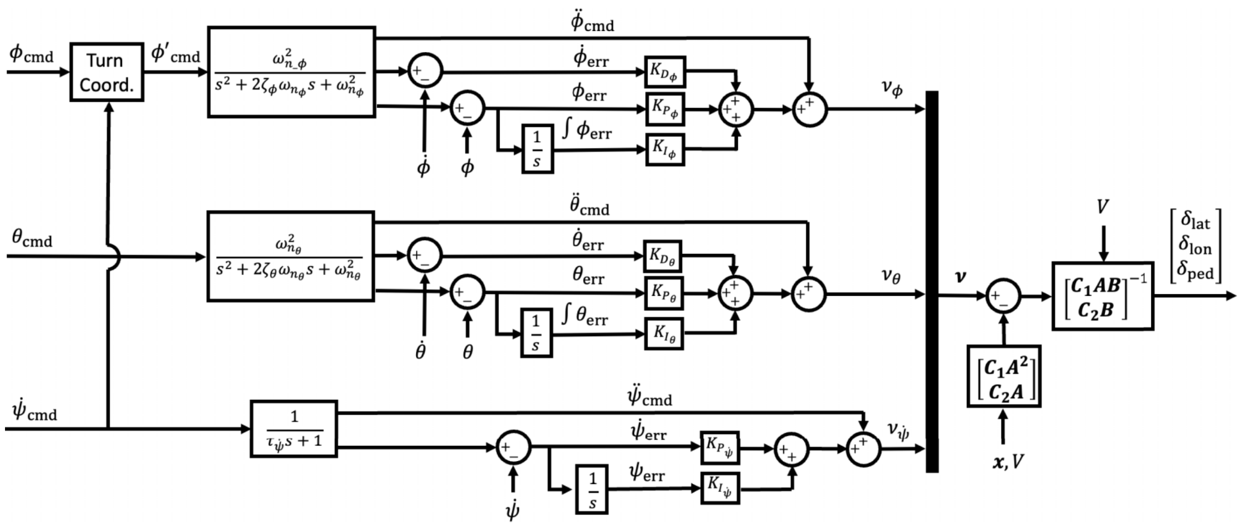

Fig. 4. Schematic of the inner-attitude loop.

such that the velocities in the heading frame are given by

$$\begin{bmatrix}V_x\\V_y\\V_z\end{bmatrix}=\boldsymbol{T}_{B\to h}\begin{bmatrix}u\\v\\w\end{bmatrix}\tag{22}$$

The baseline outer loop control strategy is based on the following reduced-order dynamics:

$$\begin{aligned}\begin{bmatrix}\dot{u}\\\dot{v}\\\dot{w}\end{bmatrix}&=\begin{bmatrix}X_u&0&0\\0&Y_v&0\\0&0&Z_w\end{bmatrix}\begin{bmatrix}u\\v\\w\end{bmatrix}+\begin{bmatrix}0&X_\theta&X_{\delta_{\text{col}}}\\Y_{\delta_\phi}&0&0\\0&Z_\theta&Z_{\delta_{\text{col}}}\end{bmatrix}\begin{bmatrix}\phi_{\text{cmd}}\\\theta_{\text{cmd}}\\\delta_{\text{col}}\end{bmatrix}\\&=\boldsymbol{Ax}+\boldsymbol{Bu}\end{aligned}\tag{23a}$$

$$\begin{aligned}\begin{bmatrix}V_x\\V_y\\V_z\end{bmatrix}&=\begin{bmatrix}\cos\theta_0&0&\sin\theta_0\\0&1&0\\-\sin\theta_0&0&\cos\theta_0\end{bmatrix}\begin{bmatrix}u\\v\\w\end{bmatrix}\\&=\boldsymbol{Cx}\end{aligned}\tag{23b}$$

where $\boldsymbol{x},\ \boldsymbol{u}$ are the reduced-order state, control input, and output vectors used for outer-loop control design; $\boldsymbol{A},\ \boldsymbol{B},\ \boldsymbol{C}$ are the system, control, and output matrices used for outer-loop control design; $u,\ v,\ w$ are the longitudinal, lateral, and vertical velocities in the body-fixed frame; $V_x,\ V_y,\ V_z$ are the longitudinal, lateral, and vertical velocities in the heading frame; $\phi_{\text{cmd}},\ \theta_{\text{cmd}}$ are the roll and pitch attitudes commanded to the inner loop; $X_u,\ Y_v,\ Z_W,\ X_\theta,\ Y_{\delta_\phi},\ Z_\theta$ are stability derivatives; $X_{\delta_{\text{col}}},\ Z_{\delta_{\text{col}}}$ are stability derivatives; and θ_0 is the trim pitch attitude.

Then, the DI outer-loop control law will be of the following form:

$$\boldsymbol{u}=(\boldsymbol{CB})^{-1}(\boldsymbol{\nu}-\boldsymbol{CAx})\tag{24}$$

where $\boldsymbol{\nu}$ is the pseudo-control vector. The first outer loop strategy is shown in Fig. 5(a).

The outer loop control strategy making use of redundant control allocation is based on Ref. 16, where the auxiliary control input (commanding the pusher propellers' collective pitch) is included as a control variable:

$$\begin{aligned}\begin{bmatrix}\dot{u}\\\dot{v}\\\dot{w}\end{bmatrix}&=\begin{bmatrix}X_u&0&0\\0&Y_v&0\\0&0&Z_w\end{bmatrix}\begin{bmatrix}u\\v\\w\end{bmatrix}+\begin{bmatrix}0&X_\theta&X_{\delta_{\text{col}}}&X_{\delta_{\text{aux}}}\\Y_{\delta_\phi}&0&0&0\\0&Z_\theta&Z_{\delta_{\text{col}}}&Z_{\delta_{\text{aux}}}\end{bmatrix}\begin{bmatrix}\phi_{\text{cmd}}\\\theta_{\text{cmd}}\\\delta_{\text{col}}\\\delta_{\text{aux}}\end{bmatrix}\\&=\boldsymbol{Ax}+\bar{\boldsymbol{B}}\boldsymbol{u}\end{aligned}\tag{25}$$

Because the controlled variables are now three (i.e., V_x, V_y, and V_z) whereas the control inputs are four (i.e., ϕ_{cmd}, θ_{cmd}, δ_{col}, and δ_{aux}), $\bar{\boldsymbol{B}}\in\mathbb{R}^{3\times 4}$ such that $\boldsymbol{C}\bar{\boldsymbol{B}}\in\mathbb{R}^{4\times 3}$ will no longer be square and thus invertible. To address this problem, a pseudo-inverse control strategy is adopted (Refs. 51, 52). The outer loop control vector is reformulated as

$$\boldsymbol{u}=\boldsymbol{Gd}\tag{26}$$

where $\boldsymbol{G}\in\mathbb{R}^{4\times 3}$ is the control allocation matrix and $\boldsymbol{d}^T=[\phi_{\text{cmd}}\ \theta_{\text{cmd}}\ \delta_{\text{col}}]$ is the pseudo-control vector. The control allocation is defined as

$$\boldsymbol{G}=\boldsymbol{W}_{\text{s}}^{-1}\bar{\boldsymbol{B}}^T\left(\bar{\boldsymbol{B}}\boldsymbol{W}_{\text{s}}^{-1}\bar{\boldsymbol{B}}^T\right)^{-1}\tag{27}$$

The weighting matrix $\boldsymbol{W}_{\text{s}}$ is defined as

$$\boldsymbol{W}_{\text{s}}=\boldsymbol{S}^T\boldsymbol{WS}\tag{28}$$

where $\boldsymbol{W}\in\mathbb{R}^{4\times 4}$ is a diagonal weighting matrix used to assign different costs to specific effectors and $\boldsymbol{S}\in\mathbb{R}^{4\times 4}$ is a scaling matrix that accounts for the different units of the control input. Then the DI outer loop control law, becomes

$$\boldsymbol{u}=\boldsymbol{G}\left(\boldsymbol{C}\bar{\boldsymbol{B}}\boldsymbol{G}\right)^{-1}(\boldsymbol{\nu}-\boldsymbol{CAx})\tag{29}$$

This second outer loop strategy is shown in Fig. 5(b).

Like for the inner-velocity loop, the stability and control derivatives are a function of the total speed V, such that the coefficient matrices $(\boldsymbol{CB})^{-1}$, $(\boldsymbol{C}\bar{\boldsymbol{B}}\boldsymbol{G})^{-1}$, and $\boldsymbol{CA}$ are also functions of total speed. Thus, these matrices are computed at discrete speed increments and stored offline along with those of the inner loop. The reference trajectory is subtracted from the output to find the error, which is compensated by a PI controller. The feed-forward signal is subsequently added, leading to the pseudo-control vector for the outer loop:

$$\begin{bmatrix}\nu_{V_x}\\\nu_{V_y}\\\nu_{V_z}\end{bmatrix}=\begin{bmatrix}\dot{V}_{V_{x_{\text{cmd}}}}\\\dot{V}_{V_{y_{\text{cmd}}}}\\\dot{V}_{V_{z_{\text{cmd}}}}\end{bmatrix}+\boldsymbol{K}_P\begin{bmatrix}e_{V_x}\\e_{V_y}\\e_{V_z}\end{bmatrix}+\boldsymbol{K}_I\begin{bmatrix}\int e_{V_x}dt\\\int e_{V_y}dt\\\int e_{V_z}dt\end{bmatrix}\tag{30}$$

where $\boldsymbol{K}_P\in\mathbb{R}^{3\times 3}$ and $\boldsymbol{K}_I\in\mathbb{R}^{3\times 3}$ are proportional and integral gain matrices, respectively. The command models for the longitudinal, lateral, and vertical speed are first order, and their break frequencies are reported in Table 3.

The error dynamics is compensated for by PI or PID control strategies, depending on the order of the command filter, as articulated in

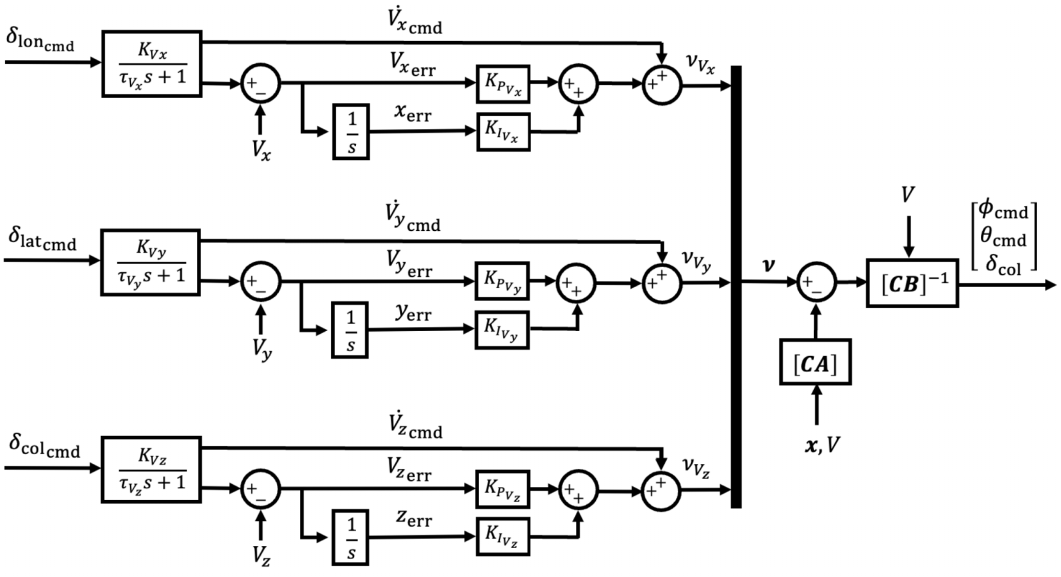

(a) Baseline

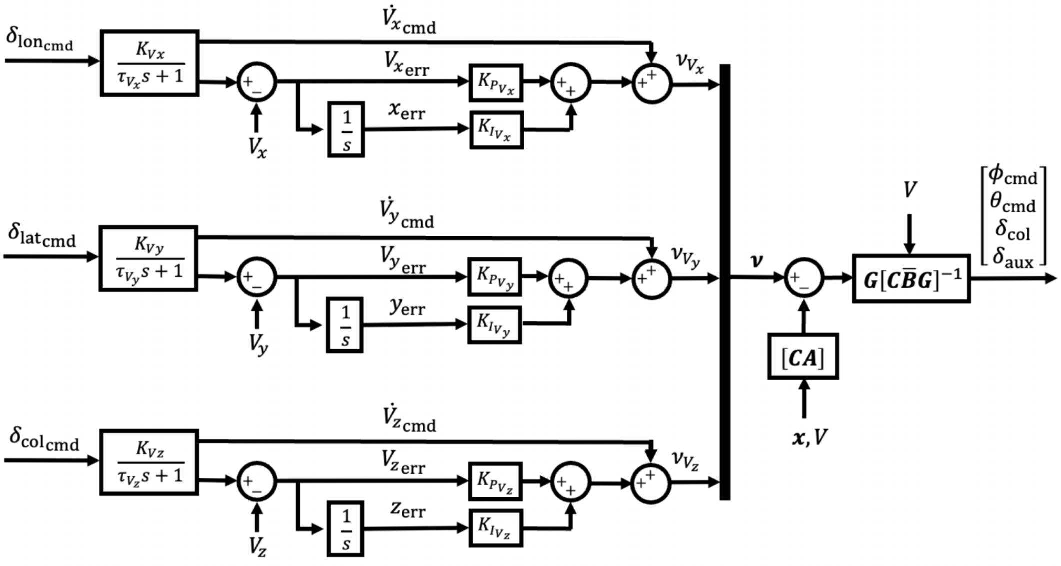

(b) Pseudo inverse (PI)

Fig. 5. Schematic of the outer-velocity loops.

Table 3. Outer loop command models properties.

	$\tau(s)$
$V_{x_{\text{cmd}}}$	1
$V_{y_{\text{cmd}}}$	1
$V_{z_{\text{cmd}}}$	0.5

Table 4. Inner loop disturbance rejection frequencies, damping ratios, and integrator poles.

	ω_n(rad/s)	ζ	p
ϕ_{cmd}	4.5	0.7	0.75
θ_{cmd}	4.0	0.7	0.75
r_{cmd}	1	0.7	–

Table 5. Outer loop disturbance rejection frequencies and damping ratios.

	ω_n(rad/s)	ζ
$V_{x_{\text{cmd}}}$	1	1
$V_{y_{\text{cmd}}}$	1	1
$V_{z_{\text{cmd}}}$	2	1

Refs. 16, 28–30, 39, 41, 42, 44, and 53. Tables 4 and 5 show the natural frequencies, damping ratios, and the integrator pole values used to compute the inner and outer loop PI/PID gains.

Turn coordination

Because the tilt-rotor/wing flight envelope includes low-speed flight (i.e., lower than approximately 50 kt) as well as high-speed flight (i.e.,

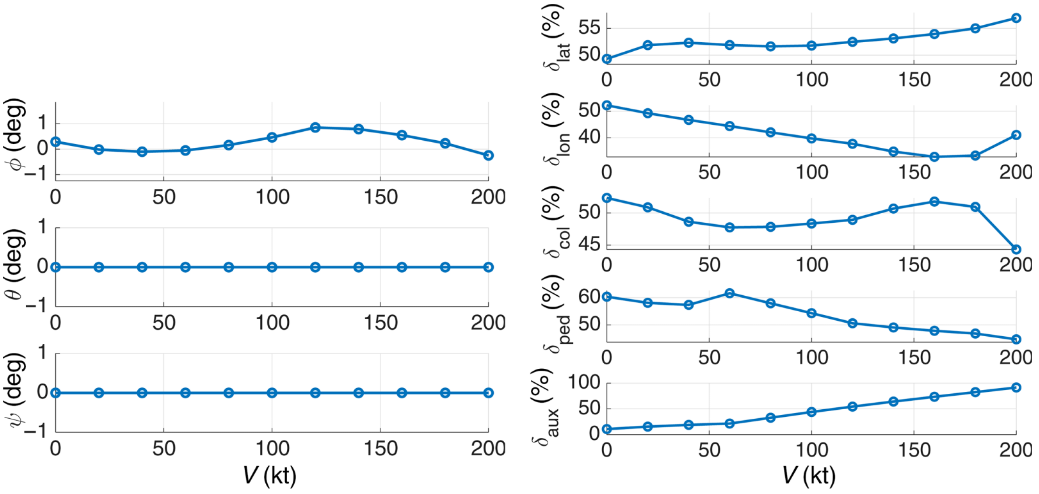

(a) Euler angles **(b)** Control inceptors

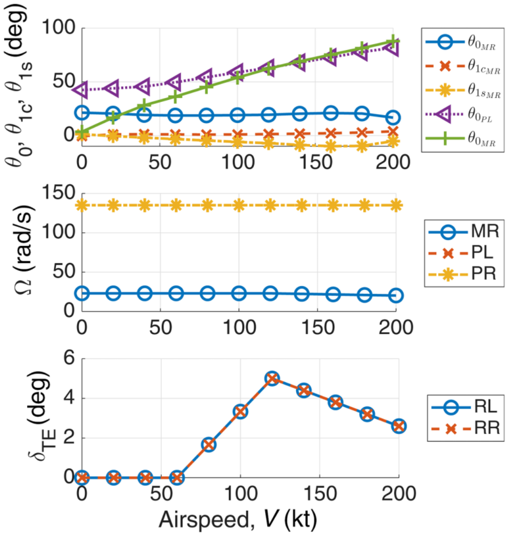

(c) Control effectors

Fig. 6. Trim variables for increasing speed.

greater than 50 kt), different control strategies are necessary to control the yaw rate for these two flight conditions. Above 50 kt, turn coordination is used; below 50 kt, no turn coordination (Ref. 54) is used. These control strategies are summarized as follows:

$$\phi'_{\text{cmd}} = \begin{cases} \phi_{\text{cmd}}, & V < V_{\text{HS}} \\ \tan^{-1}\left(\frac{V}{g}\dot{\psi}_{\text{cmd}}\right), & V \geq V_{\text{HS}} \end{cases} \tag{31}$$

where $V_{\text{HS}} = 50$ kt.

Results

Trim

As a first step, the simulation model is from 0 to 200 kt. Because the scheduling of the auxiliary pilot stick with speed (equivalently, the scheduling of the pusher propellers collective pitch with speed) is unknown, the auxiliary control input is used as a control variable in place of the pitch attitude. More specifically, the pitch attitude is prescribed to zero while the auxiliary control input is an unknown variable in the trim process. The trim attitude and pilot control inputs are shown in Fig. 6. More specifically, Fig. 6(a) shows the trim Euler angles for increasing flight speed. While trim pitch and yaw attitudes are zero across the flight speed considered, which stems from trimming with zero pitch attitude and sideslip, the trim roll attitude is not zero due to the asymmetric use of the pusher propellers, which leads to asymmetric torque about the longitudinal axis. The asymmetric torque is explained by the fact that, to counteract the main rotor torque, at least at hover, the right propeller will have to "pull" whereas the left propeller will have to "push." In any case, the resulting trim roll attitude is small (less than 1 deg) and across the trim envelope considered. Figure 6(b) shows the trim control inputs for increasing speed. In this figure, all four conventional pilot sticks are shown to remain approximately neutral—which also stems from the chosen control mixing. The auxiliary control input increases somewhat linearly between 0 and 60 kt and also linearly but with a different slope from 60 to 200 kt. While the control mixing matrices are not reported for brevity, the trim actuator inputs are shown in Fig. 6(c). The trim collective pitch of the main rotor ($\theta_{0_{MR}}$) is shown to mimic the power curve up to approximately 140 kt, for it not to increase but rather decrease at higher speeds as the necessary propulsive force is provided by the pusher propellers. This figure also shows how the main rotor speed drops from 23.04 to 19.58 rad/s from 120 to 160 kt. Finally, prescribed rudder trim tab

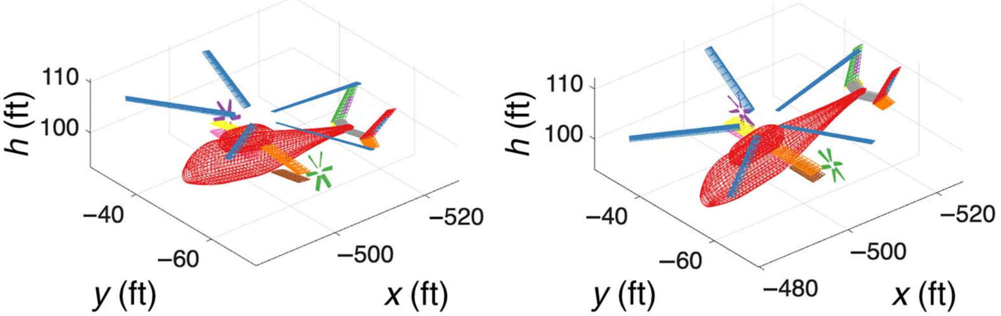

(a) $\theta = 10$ deg **(b)** $\theta = -10$ deg

Fig. 7. Trim at arbitrary pitch attitudes.

Table 6. Trim rotor control inputs and rotor forces and moments for hovering at varying pitch attitudes

Parameter	Value			Units
	0 deg	10 deg	−10 deg	
Controls				
$\theta_{0_{MR}}$	21.36	21.20	21.20	deg
$\theta_{1c_{MR}}$	−0.4	−0.93	0.07	deg
$\theta_{1s_{MR}}$	1.29	1.24	1.30	deg
$\theta_{0_{PR}}$	42.47	55.71	16.13	deg
$\theta_{0_{PL}}$	3.61	2.33	−9.04	deg
Forces				
$\{X,\ Y,\ Z\}_{MR}$	{325, −60.4, −11905}	{318, −178, −11723}	{327, 44.7, −11724}	lb
$\{X,\ Y,\ Z\}_{PR}$	{759, 0, 0}	{1779, 0, 0}	{−296, 0, 0}	lb
$\{X,\ Y,\ Z\}_{PL}$	{−1084, 0, 0}	{−29.8, 0, 0}	{−2098, 0, 0}	lb
Moments				
$\{L,\ M,\ N\}_{MR}$	{618.2, 1951, 22414}	{−195.7, 1909, 21998}	{1307, 1963, −21924}	lb-ft
$\{L,\ M,\ N\}_{PR}$	{388.7, 0, 0}	{1326, 0, 0}	{114.2, 0, 0}	lb-ft
$\{L,\ M,\ N\}_{PL}$	{−644.0, 0, 0}	{−62.5, 0, 0}	{−1689, 0, 0}	lb-ft

inputs are used above 60 kt to at least partially counteract the main rotor torque in forward flight.

Next, the capability to hover at arbitrary pitch attitudes—which is particularly important for target acquisition and tracking and is enabled only in rotorcraft equipped with auxiliary propulsion units—is demonstrated in Fig. 7. These results were obtained by prescribing the trim pitch attitude to ±10 deg and solving for the trim pilot inputs, including the auxiliary pilot stick. The corresponding rotor actuator inputs, as well as the rotor forces and moments about each rotor hub (expressed in the body frame), are summarized in Table 6.

Handling qualities

Closed-loop performance is assessed in the frequency domain by evaluating selected stability, performance, and handling-quality metrics. For brevity, only hover results are presented in this analysis. This evaluation considers the following components: (i) a flight control computer operating at 100 Hz, resulting in a processing delay and a digital-to-analog sample-and-hold delay of $\tau = 50$ ms each; (ii) actuators modeled with second-order dynamics and bandwidths of 8 Hz (approximately 50.27 rad/s); (iii) sensors represented as second-order filters with bandwidths of 10 Hz (equivalently, 31.42 rad/s); and (iv) an additional sensor transport delay of $\tau = 20$ ms to account for sampling skew and bus transport delays (Ref. [55]).

The first metrics evaluated are the gain and phase margins (GM/PM), commonly referred to as stability margins, which are associated with the on-axis broken-loop response. According to Ref. 56, Level 1 handling qualities are achieved when the broken-loop response satisfies a gain margin of at least 4 dB and a phase margin of at least 45 deg. The gain and phase margins for all controlled axes in the inner attitude and outer velocity loops are presented in Fig. 8. As shown, the stability margins generally meet the specified criteria for all aircraft, with the exception of the roll-axis inner loop, where the phase margin is approximately 20 deg.

The second set of metrics assessed includes the disturbance rejection bandwidth (DRB) and disturbance rejection peak (DRP) (Ref. [57]). The performance requirements for these metrics vary across different control axes. The results, shown in Fig. 9, indicate that the DRB/DRP criteria are generally satisfied, except in the roll and pitch axes, where the DRP slightly exceeds the specified thresholds—suggesting somewhat reduced disturbance rejection performance in those channels. Notably, the DRB/DRP performance of the PI control law closely matches that of the baseline controller across most axes. However, the PI configuration achieves a significantly lower (i.e., improved) DRP in the longitudinal velocity axis, indicating enhanced disturbance rejection. This improvement is attributed to the redistribution of control effort to the pusher propellers, which provides additional means for attenuating longitudinal disturbances.

The third and final set of results compares the closed-loop response with the command models used for each axis in the frequency domain. These results, presented in Fig. 10, generally demonstrate good on-axis tracking performance across all axes and aircraft. However, in the longitudinal and lateral speed channels, the baseline control law shows

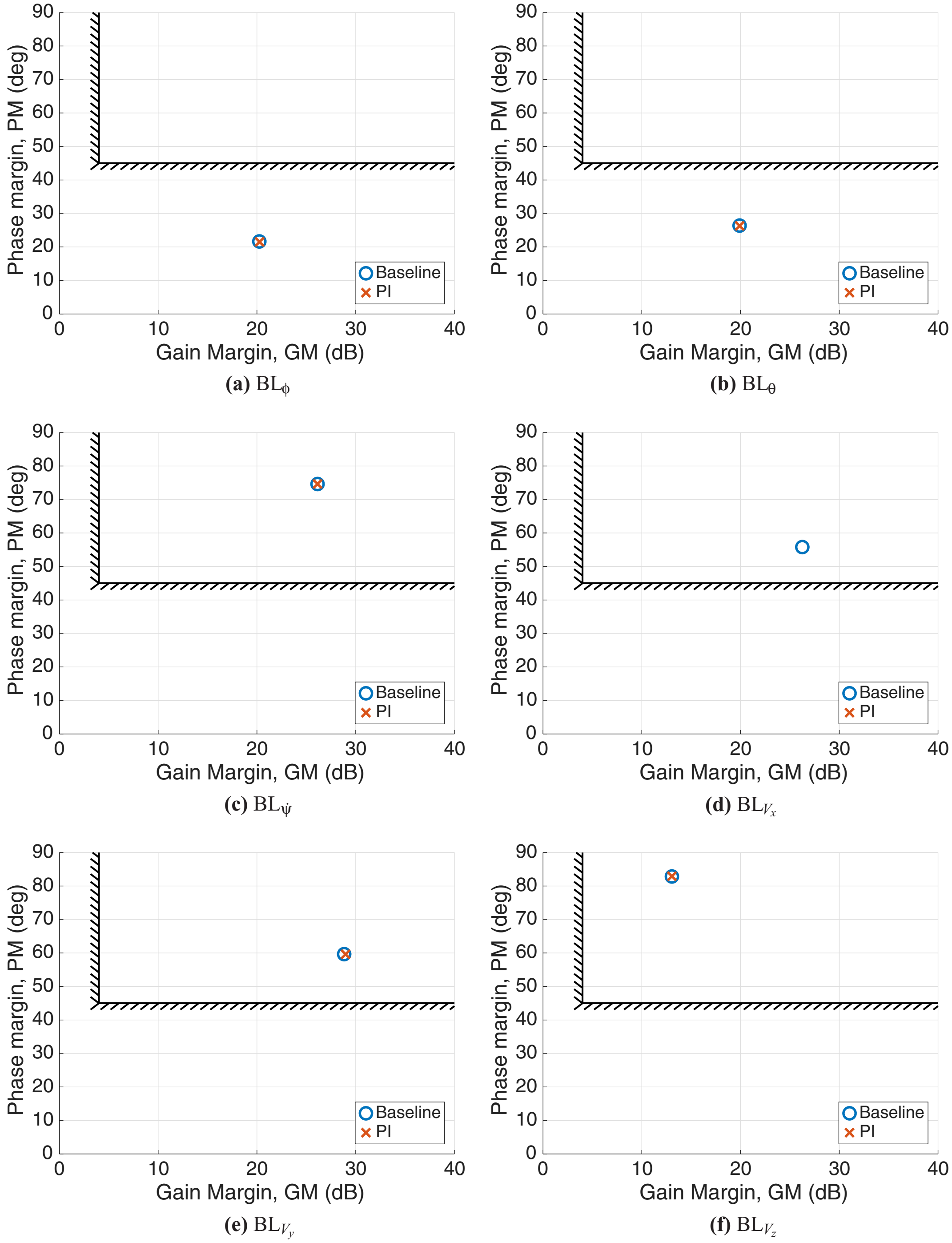

(a) BL$_\phi$ **(b)** BL$_\theta$

(c) BL$_{\dot\psi}$ **(d)** BL$_{V_x}$

(e) BL$_{V_y}$ **(f)** BL$_{V_z}$

Fig. 8. Hover stability margins.

noticeable degradation in the command model following above approximately 1 rad/s, as illustrated in Figs. 10(d) and 10(e). In contrast, the PI control law closely matches the command model across the full frequency range in the longitudinal axis, indicating a substantial improvement in closed-loop response at higher frequencies. Overall, these results confirm that the control system design provides satisfactory performance in terms of stability, disturbance rejection, and reference tracking within the defined operational envelope, with the PI configuration exhibiting improved command model tracking in the longitudinal speed response.

Hover-to-cruise transition

The rotorcraft flight dynamics are linearized and residualized at each discrete speed increment to obtain the coefficient matrices for the DI control laws. The PI control law is formulated to allocate the majority of control effort to the auxiliary control input. As a result, during acceleration, the rotorcraft governed by the PI control law relies primarily on the thrust produced by the pusher propellers, rather than pitching forward to reorient the main rotor thrust vector. The scaling matrix used for these

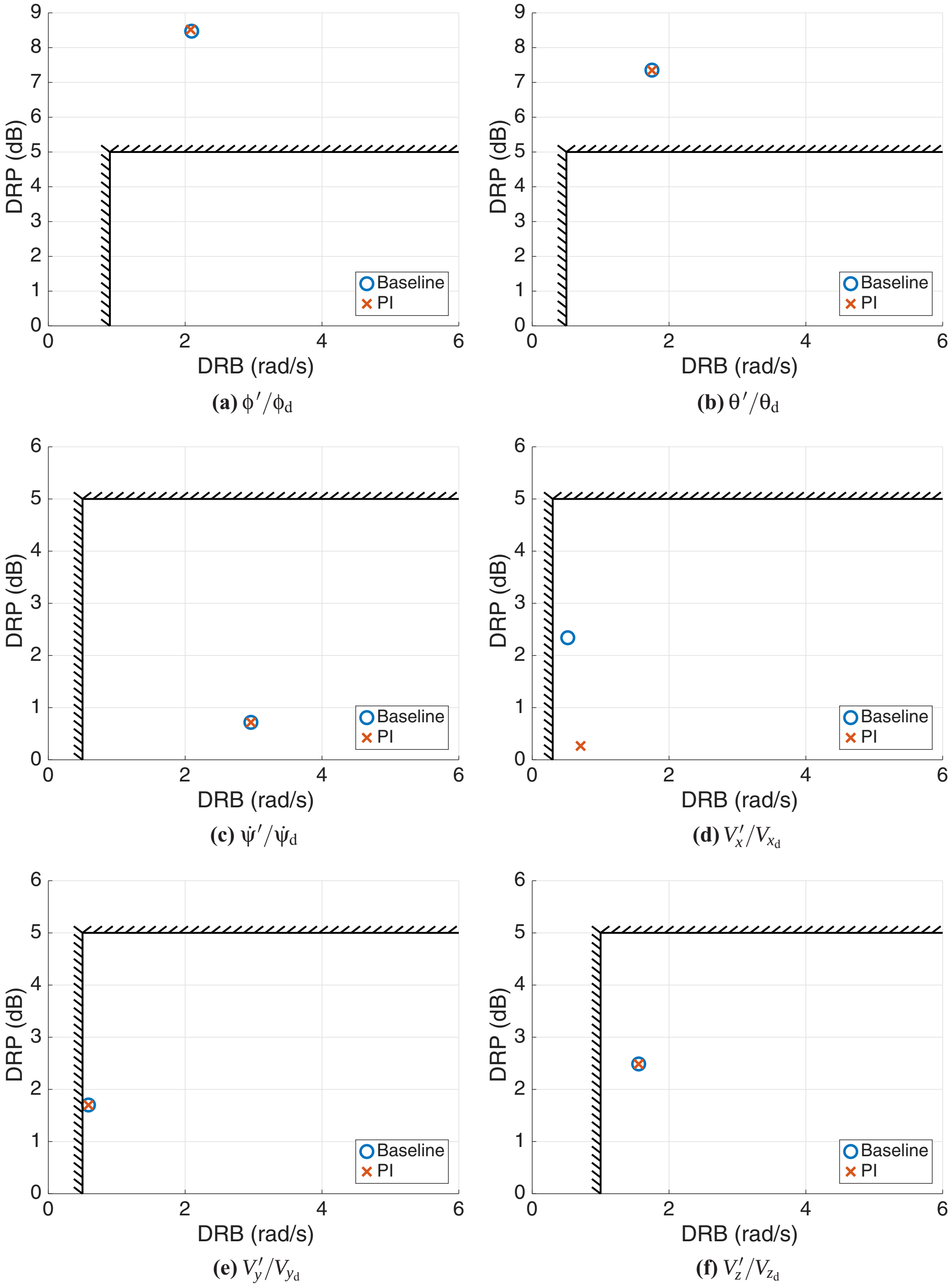

(a) ϕ'/ϕ_{d} **(b)** $\theta'/\theta_{\mathrm{d}}$

(c) $\dot{\psi}'/\dot{\psi}_{\mathrm{d}}$ **(d)** $V_x'/V_{x_{\mathrm{d}}}$

(e) $V_y'/V_{y_{\mathrm{d}}}$ **(f)** $V_z'/V_{z_{\mathrm{d}}}$

Fig. 9. Hover disturbance rejection bandwidth and peak (DRP/DRB).

control laws is defined as

$$\boldsymbol{S} = \mathrm{diag}\left(\left[\frac{180}{\pi} \;\; \frac{180}{\pi} \;\; 1 \;\; 1\right]\right), \tag{32}$$

such that 1 deg of roll or pitch attitude corresponds to 1% of collective or auxiliary stick input. The weighting matrix is selected such that its trace (i.e., the sum of its diagonal elements) equals the matrix order, ensuring that the overall weight distribution remains normalized. For control axes with redundant effectors, the individual diagonal entries corresponding to those actuators may be increased or decreased to bias control allocation, provided that their sum remains equal to the number of redundant effectors for that axis. This preserves the net authority assigned to each axis while allowing redistribution among actuators. The weighting matrix used in this example to bias the control effort toward the auxiliary control input is

$$\boldsymbol{W} = \mathrm{diag}([1 \;\; 0.1 \;\; 1 \;\; 1.9]) \tag{33}$$

These control laws are demonstrated through a closed-loop simulation of an acceleration from hover to cruise flight. The maneuver consists of an acceleration from hover to 160 kt over 40 s, using the full nonlinear rotorcraft model. Figure 11(a) shows the heading-frame velocity

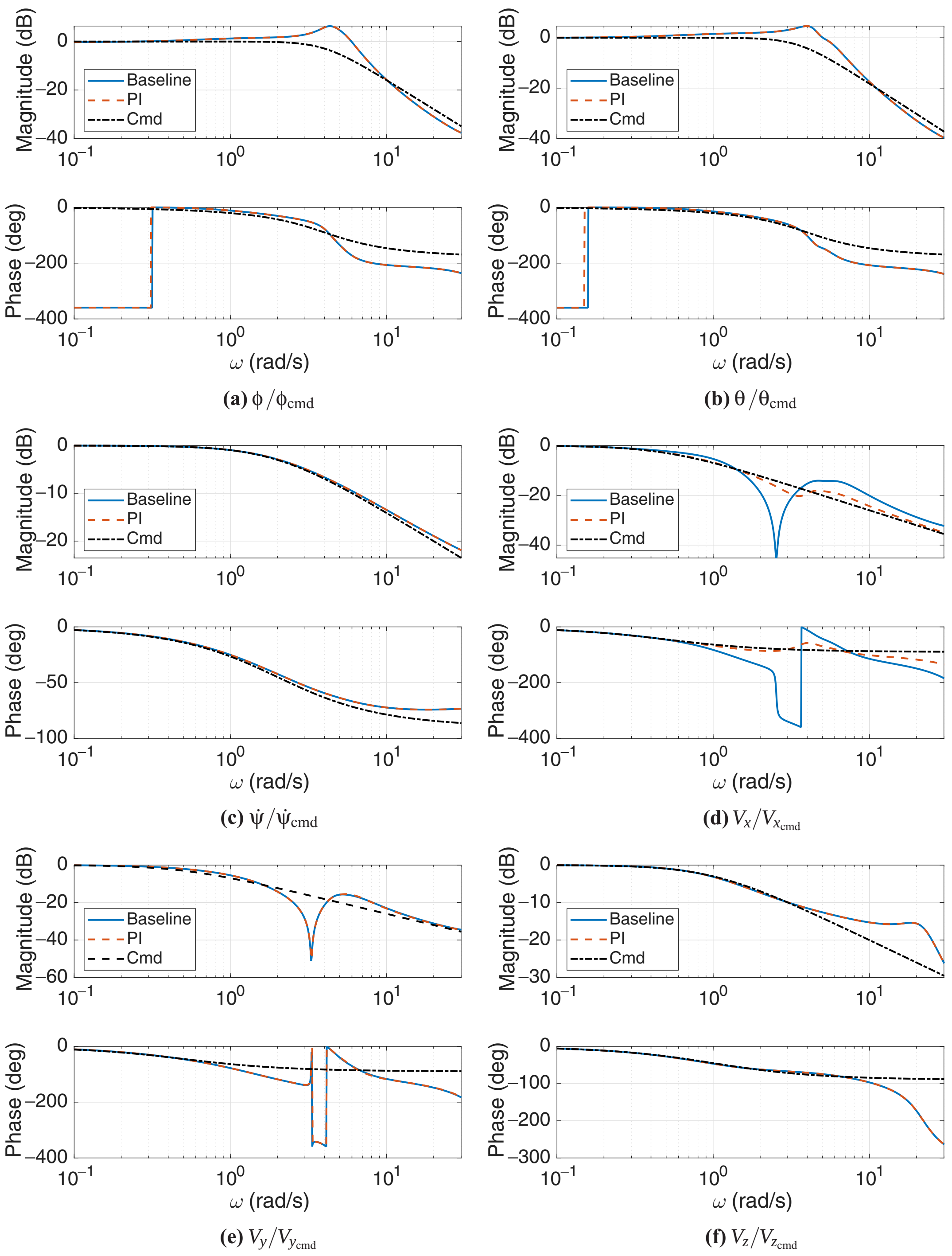

(a) ϕ/ϕ_{cmd} **(b)** $\theta/\theta_{\mathrm{cmd}}$

(c) $\dot{\psi}/\dot{\psi}_{\mathrm{cmd}}$ **(d)** $V_x/V_{x_{\mathrm{cmd}}}$

(e) $V_y/V_{y_{\mathrm{cmd}}}$ **(f)** $V_z/V_{z_{\mathrm{cmd}}}$

Fig. 10. Hover on-axis closed-loop responses compared to the command models.

components. The longitudinal velocity accurately tracks the reference trajectory, while off-axis deviations in lateral velocity remain minimal for both the baseline and PI control laws. The vertical velocity response shows a brief deviation from zero for the baseline controller during deceleration at approximately 36 s. This occurs because the rotorcraft pitches up to decelerate, thereby gaining vertical speed. This effect is absent in the PI control law, which reduces acceleration by decreasing thrust from the pusher propellers while maintaining pitch attitude. The closed-loop attitude response, shown in Fig. 11(b), confirms that the inner attitude loop effectively tracks the commanded pitch while maintaining near-zero roll and yaw angles. The baseline control law yields a pitch attitude reduction to approximately −15 deg to direct main rotor thrust forward for acceleration. In contrast, the PI control law maintains a pitch attitude closer to −3 deg by reallocating control effort to the pusher propellers. This reallocation is illustrated in Fig. 11(c), where the baseline controller uses more longitudinal stick input, while the PI controller employs less stick input but more auxiliary control input starting at the onset of the maneuver. The corresponding actuator inputs are shown in Figs. 11(d) and

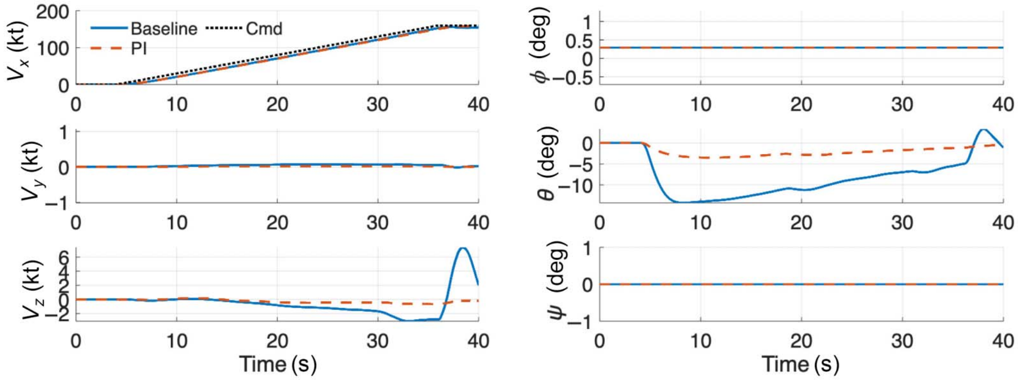

(a) Heading-frame velocities **(b)** Euler angles

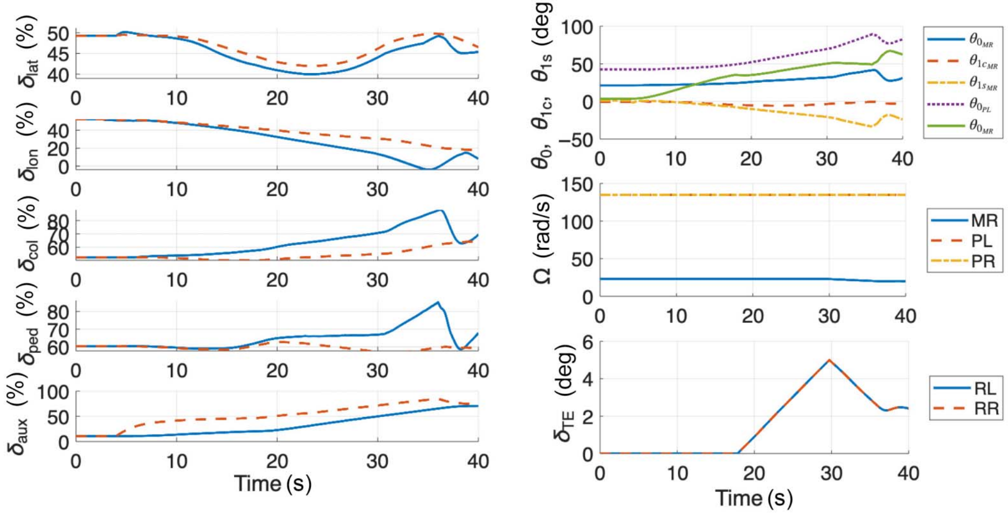

(c) Control inceptors **(d)** Control effectors (baseline)

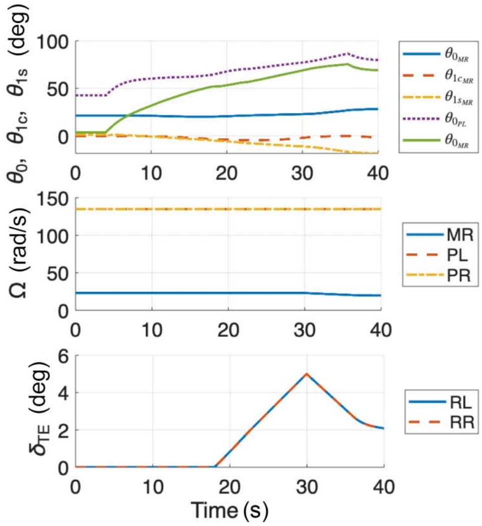

(e) Control effectors (pseudo-inverse)

Fig. 11. Acceleration from 0 to 80 kt with different control allocation strategies.

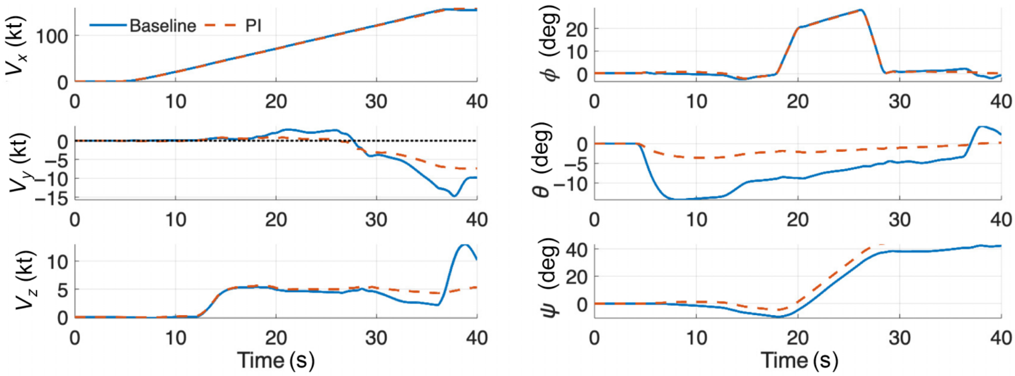

(a) Heading-frame velocities **(b)** Euler angles

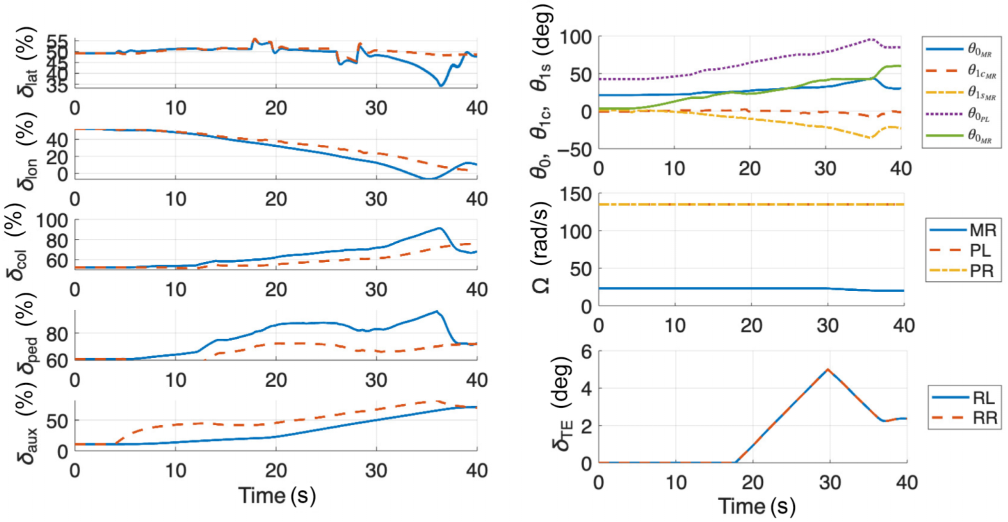

(c) Control inceptors **(d)** Control effectors (baseline)

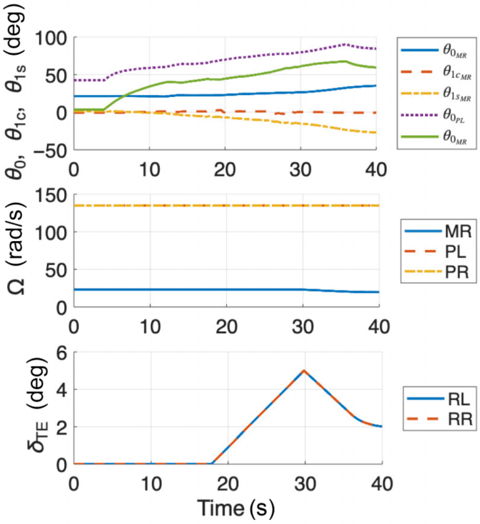

(e) Control effectors (pseudo-inverse)

Fig. 12. Actuator inputs for an acceleration from 0 to 80 kt with different control allocation strategies.

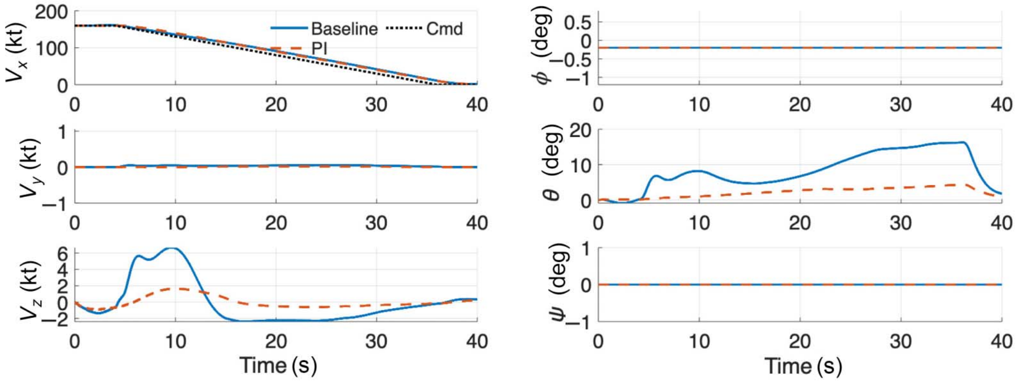

(a) Heading-frame velocities

(b) Euler angles

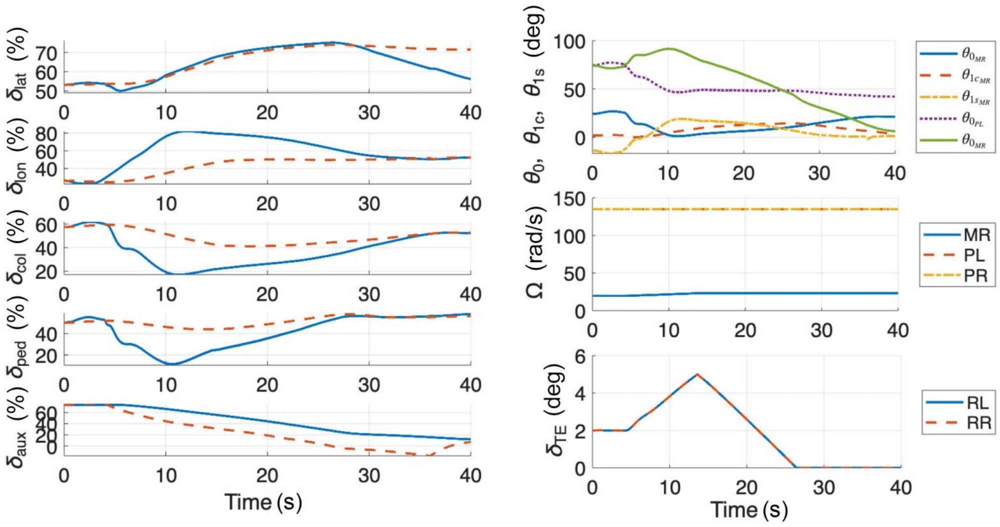

(c) Control inceptors

(d) Control effectors (baseline)

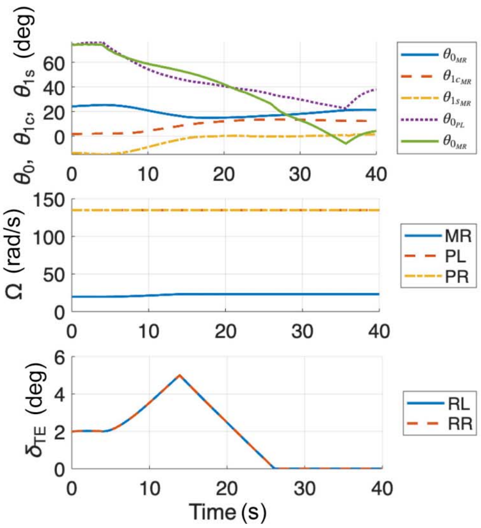

(e) Control effectors (pseudo-inverse)

Fig. 13. Automatic transition from hover (helicopter mode) to high-speed forward flight (airplane mode).

11(e), where the PI controller reduces the main rotor longitudinal cyclic input and increases collective inputs to the left and right propellers.

A second 60-s transition simulation, consisting of an acceleration from hover to cruise flight (160 kt) while simultaneously performing a turn and a 600 ft/min climb, is shown in Fig. 12 to evaluate the performance of the flight control laws in the lateral axis. The rotorcraft begins in a hover condition and initiates acceleration at the fourth second of the simulation. At the 12th second, the climb begins at 600 ft/min, and at approximately 17.5 s, the rotorcraft enters a coordinated right turn at a yaw rate of $\dot{\psi} = 0.1$ rad/s. Since the rotorcraft is accelerating and the bank angle required for turn coordination is given by $\phi = \mathrm{atan}\left(\frac{\dot{\psi}V}{g}\right)$, the bank angle ϕ increases as airspeed V increases during the turn. The acceleration and turn are maintained until second 36, while the climb rate is sustained until the end of the simulation.

Cruise-to-hover transition

A third 40-s closed-loop simulation, consisting of a reverse transition from cruise flight at 160 kt to hover, is presented to demonstrate the capability of the control laws to handle reverse transitions as well. This simulation is illustrated in Fig. 13. As shown, the baseline control law induces a nose-up pitch attitude during deceleration (Fig. 13(b)), whereas the PI control law maintains a near-zero pitch attitude by relying on the propellers to decelerate (Figs. 13(c) and 13(e)). Overall, both control laws achieve comparable on-axis tracking performance; however, off-axis performance—particularly in the vertical velocity response—is improved with the PI control law, which results in reduced vertical speed excursions.

Conclusions

This study presented the development, implementation, and evaluation of DI flight control laws for a compound rotorcraft configuration representative of the Airbus RACER. The DI control laws were structured within a multiloop architecture and incorporated redundant control allocation to the auxiliary propulsion units via a pseudo-inverse (PI) strategy. A generic multirotor/wing simulation model was adapted to model the flight dynamics of the RACER configuration. The model was trimmed and linearized at discrete speeds from hover to cruise, and control reallocation was used to enable trimming at zero pitch attitudes. Control reallocation for trimming at arbitrary pitch attitudes at hover was also demonstrated. Model-order reduction techniques in the form of residualization were applied to derive reduced-order models suitable for control design. Both a baseline DI controller and a PI variant were implemented and evaluated in closed-loop simulations using the full-order nonlinear dynamics. Three representative maneuvers were considered: (i) a hover-to-cruise transition, (ii) a combined transition, climb, and coordinated turn, and (iii) a reverse transition from cruise to hover. In addition, frequency-domain metrics related to stability, performance, and handling qualities were assessed for both control laws. Based on these results, the following conclusions can be drawn:

1) Dynamic inversion relies on model inversion to cancel the plant dynamics and track a desired reference model by consolidating scheduling into the plant model, thereby reducing gain scheduling and overall controller complexity. This approach, however, requires accurate, flight-condition-dependent characterization of the plant.

2) Control allocation to the propellers enabled trimming at prescribed pitch attitudes in hover and at zero pitch attitude and heading in forward flight, with minor roll deviations due to asymmetric propeller torque. This capability offers flexibility for missions requiring fixed attitude profiles, such as hover target acquisition and tracking or sensor pointing.

3) Active allocation of the control signal to the redundant control effectors—specifically, the pusher propellers—enabled the minimization of pitch attitude variations during acceleration and deceleration maneuvers. This approach improved tracking performance compared to conventional control laws and achieved comparable handling-quality metrics. Minimizing pitch excursions may also enhance passenger comfort in operational scenarios.

4) Redundant control allocation to the pusher propellers improved longitudinal speed disturbance rejection and command model following. The PI control law achieved a lower disturbance rejection peak and more accurate closed-loop tracking, particularly above 1 rad/s.

5) By decoupling longitudinal thrust generation from pitch attitude changes, active control allocation to the auxiliary propulsion system enables trimming at arbitrary pitch attitudes and minimizes pitch excursions during acceleration and deceleration maneuvers.

Acknowledgments

The author would like to thank Dr. Tomasz Krysinski for his assistance in shaping the scope of the paper.

References

[1] Lopez, M. J. S., Padthe, A. K., Glover, E. D., Berger, T., and Tobias, E. L., "Seeking Lift Share: Design Tradeoffs for a Winged Single Main Rotor Helicopter," Proceedings of the 78th Annual Forum of the Vertical Flight Society, Fort Worth, TX, May 10–12, 2022, doi: https://doi.org/10.4050/F-0078-2022-17547.

[2] Padthe, A. K., Lopez, M. J. S., Berger, T., Juhasz, O., Tobias, E. L., and Glover, E. D., "Design, Modeling, and Flight Dynamics Analysis of Generic Lift-Offset Coaxial Rotor Configurations," Proceedings of the 78th Annual Forum of the Vertical Flight Society, Fort Worth, TX, May 10–12, 2022, doi: https://doi.org/10.4050/F-0078-2022-17580.

[3] Berger, T., Juhasz, O., Lopez, M. J. S., Tischler, M. B., and Horn, J. F., "Modeling and Control of Lift Offset Coaxial and Tiltrotor Rotorcraft," Proceedings of the 44th European Rotorcraft Forum 2018 (ERF 2018), Delft, the Netherlands.

[4] Berger, T., Juhasz, O., Lopez, M. J. S., Tischler, M. B., and Horn, J. F., "Modeling and Control of Lift Offset Coaxial and Tiltrotor Rotorcraft," *CEAS Aeronautical Journal*, Vol. 11, 2024, pp. 191–215, doi: https://doi.org/10.1007/s13272-019-00414-0.

[5] Straubinger, A., Rothfeld, R., Shamiyeh, M., Bütcher, K. D., Kaiser, J., and Plötner, K. O., "An Overview of Current Research and Developments in Urban Air Mobility – Setting the Scene for UAM Introduction," *Journal of Air Transport Management*, **87**, 101852 (2020), doi: https://doi.org/10.1016/j.jairtraman.2020.101852.

[6] Sliva, C., Johnson, W., Antcliff, K. R., and Patterson, M. D., "VTOL Urban Air Mobility Concept Vehicles for Technology Development," AIAA 2018-3847, Proceedings of the 2018 Aviation Technology, Integration, and Operations Conference, Atlanta, GA, June 25–29, 2018, doi: https://doi.org/10.2514/6.2018-3847.

[7] Thiemeier, J., Ohrle, C., Frey, F., Keßler, E., and Kramer, E., "Aerodynamics and Flight Mechanics Analysis of Airbus Helicopters' Compound Helicopter RACER in Hover Under Crosswind Conditions," *CEAS Aeronautical Journal*, Vol. 11, 2020, pp. 49–66, doi: https://doi.org/10.1007/s13272-019-00392-3.

[8] Frey, F., Thiemeier, J., Ohrle, C., Keßler, E., and Kramer, E., "Aerodynamic Interactions on Airbus Helicopters' Compound Helicopter RACER in Cruise Flight," *Journal of the American Helicopter Society*, **65**, 042001 (2020), doi: https://doi.org/10.4050/JAHS.65.042001.

[9] Frey, F., Thiemeier, J., Ohrle, C., Keßler, E., and Kramer, E., "Aerodynamic Interactions on Airbus Helicopters' Compound Helicopter RACER in Hover," *Journal of the American Helicopter Society*, **67**, 012007 (2022), doi: https://doi.org/10.4050/JAHS.67.012007.

[10] Ohrle, C., Frey, F., Thiemeier, J., Keßler, E., and Kramer, E., "Coupled and Trimmed Aerodynamic and Aeroacoustic Simulations for Airbus Helicopters' Compound Helicopter RACER," *Journal of the American Helicopter Society*, **64**, 032003 (2019), doi: https://doi.org/10.4050/JAHS.64.032003.

[11] Lienard, C., Salah el Din, I., Renaud, T., and Fukari, R., "RACER High-Speed Demonstrator: Rotor and Rotor-Head Wake Interactions with Tail Unit," Proceedings of the 74th Annual Forum of the American Helicopter Society, Phoenix, AZ, May 14–17, 2018, doi: https://doi.org/10.4050/F-0074-2018-16058.

[12] Salah el Din, I., Lienard, C., Huot, R., and Fukari, R., "RACER High-Speed Demonstrator: Tail Unit Vertical Fin Aerodynamic Design," Proceedings of the 74th Annual Forum of the American Helicopter Society, Phoenix, AZ, May 14–7, 2018, doi: https://doi.org/10.4050/F-0074-2018-12724.

[13] Horn, a. P. R. J., J. F., Bridges, D. O., Nicholas, A. K., Hagwood, D. G., Berger, T., and Gong, A., "Piloted Simulation Evaluation of Maneuver Optimization Control for a Coaxial Compound Helicopter," Proceedings of the 79th Annual Forum of the Vertical Flight Society, West Palm Beach, FL, May 16–18, 2023, doi: https://doi.org/10.4050/F-0079-2023-18077.

[14] Ozdemir, G. T., "In-Flight Performance Optimization for Rotorcraft with Redundant Controls," Ph.D. thesis, The Pennsylvania State University, University Park, PA, December 2013.

[15] Thorsen, A. T., and Horn, J. F., "Aerobatic Maneuvers of a Compound Rotorcraft at High Advance Ratios - Flight Path Generation and Dynamic Simulation," Proceedings of the AIAA Aviation Forum, Washington, DC, June 13–17, 2016, doi: https://doi.org/10.2514/6.2016-3391.

[16] Berger, T., Tischler, M. B., and Horn, J. F., "Outer-Loop Control Design and Simulation Handling Qualities Assessment for a Coaxial-Compound Helicopter and Tiltrotor," Proceedings of the 77th Annual Forum of the Vertical Flight Society, Virtual, October 5–8, 2020, doi: https://doi.org/10.4050/F-0076-2020-16392.

[17] Ozdemir, G. T., "Handling Qualities Requirements and Control Design for High-Speed Rotorcraft," Ph.D. Thesis, The Pennsylvania State University, University Park, PA, December, 2019.

[18] Saetti, U., Horn, J. F., Berger, T., and Tischler, M. B., "Handling-Qualities Perspective on Rotorcraft Load Alleviation Control," *Journal of Guidance, Control, and Dynamics*, Vol. 43, (10), 2020, pp. 1792–1804, doi: https://doi.org/10.2514/1.G004965.

[19] Ozdemir, G. T., Horn, J. F., and Thorsen, A. T., "In-Flight Multi-Variable Optimization of Redundant Controls on a Compound Rotorcraft," Proceedings of the AIAA Guidance, Navigation, and Control Conference, Boston, MA, August 19–22, 2013, doi: https://doi.org/10.2514/6.2013-5165.

[20] Tobias, E. L., and Tischler, M. B., "A Model Stitching Architecture for Continuous Full Flight-Envelope Simulation of Fixed-Wing Aircraft and Rotorcraft from Discrete-Point Linear Models," Technical Report, U.S. Army AMRDEC Special Report RDMR-AF-16-01, April 2016.

[21] Leishman, J. G., *Principles of Helicopter Aerodynamics*, Cambridge University Press, New York, NY, 2006.

[22] Pitt, D. M., and Peters, D. A., "Theoretical Prediction of Dynamic-Inflow Derivatives," Proceedings of the 6th European Rotorcraft and Powered Lift Aircraft Forum, Bristol, UK, September 16–19, 1980.

[23] Guner, F., and Prasad, J. V. R., "Combined Momentum Theory and Simple Vortex Theory Inflow Model for Multirotor Configurations," *Journal of the American Helicopter Society*, **67**, 022007 (2022), doi: https://doi.org/10.4050/JAHS.67.022007.

[24] Guner, F., "A Multirotor Inflow Model Based on Combined Momentum Theory and Simple Vortex Theory (CMTSVT) for Flight Simulations," Proceedings of the 78th Annual Forum of the Vertical Flight Society, Fort Worth, TX, May 10–12, 2022, doi: https://doi.org/10.4050/F-0078-2022-17579.

[25] Saetti, U., and Guner, F., "Interactional Aerodynamics Modeling and Flight Control Design of Multi-Rotor Aircraft," Proceedings of the 6th Decennial Aeromechanics Specialists' Conference, Santa Clara, CA, February 6–8, 2024.

[26] Jun, D., Cocco, A., Saetti, U., and Juhasz, O., "Flight Dynamics of a Coaxial Compound Helicopter with Rotor-On-Rotor Interactional Aerodynamics," Proceedings of the 50th European Rotorcraft Forum, Marseille, France, September 10–12, 2024.

[27] Hyeson, H. H., "Equations for the Induced Velocities Near a Lifting Rotor with Nonuniform Azimuthwise Vorticity Distribution," Technical Report, NASA TN D-394, 1960.

[28] Horn, J. F., "Non-Linear Dynamic Inversion Control Design for Rotorcraft," *Aerospace*, **6**, 38 (2019), doi: https://doi.org/10.3390/aerospace6030038.

[29] Saetti, U., and Horn, J. F., "Tiltrotor Simulations with Coupled Flight Dynamics, State-Space Aeromechanics, and Aeroacoustics," *Journal of the American Helicopter Society*, **69**, 012003 (2024), doi: https://doi.org/10.4050/JAHS.69.012003.

[30] Saetti, U., Horn, J. F., Lakhmani, S., Lagoa, C., and Berger, T., "Design of Dynamic Inversion and Explicit Model Following Control Laws for Quadrotor UAS," *Journal of the American Helicopter Society*, **65**, 032006 (2020), doi: https://doi.org/10.4050/JAHS.65.032006.

[31] Morcos, M. T., Luzzani, G., Fischer, M. R., Jun, D., Gary, E., Saetti, U., Geiger, D. H., Kubik, S. T., Breed, A. R., and Crane, C. J., "Full-Body Haptic Cueing for Augmented Pilot Perception in Position/Velocity Tracking Tasks," Proceedings of the 81st Annual Forum of the Vertical Flight Society, May 20–22, 2025.

[32] Saetti, U., Rinaldi, M., Guglieri, G., Berger, T., and Lu, L., "Identification of Control-Equivalent Turbulence Input (CETI) Models from Rotorcraft Simulations," Proceedings of the 81st Annual Forum of the Vertical Flight Society, May 20–22, 2025.

[33] Hillier, B. B., Stock, M. J., and Gharakhani, A., "Robust and Corrected Coefficients for the ROtor-Body-INteraction Body," *AIAA Journal*, Vol. 59, (10), 2021, pp. 4281–4283, doi: https://doi.org/10.2514/1.J060303.

[34] Mineck, R. E., and Gorton, S. A., "Steady and Periodic Pressure Measurements on a Generic Helicopter Fuselage Model in the Presence of a Rotor," Technical Report, NASA, NASA Technical Memorandum 210286, 2002.

[35] Howlett, J. J., "UH-60A Black Hawk Engineering Simulation Program. Volume 1: Mathematical Model," Technical Report, NASA-CR-166309, 1980.

[36] Ferguson, S. W., "A Mathematical Model for Real-Time Flight Simulation of Generic Tilt Rotor Aircraft," Technical Report, NASA-CR-166536, 1988.

[37] Saetti, U., and Rogers, J. D., "Revisited Harmonic Balance Trim Solution Method for Periodically-Forced Flight Vehicles," *Journal of Guidance, Control, and Dynamics*, Vol. 44, (5), May 2021, pp. 1008–1017, doi: https://doi.org/10.2514/1.G005553.

[38] Kokotovic, P. V., O'Malley, R. E., and Sannuti, P., "Singular Perturbations and Order Reduction in Control Theory, an Overview," *Automatica*, Vol. 12, (2), 1976, pp. 123–132, doi: https://doi.org/10.1016/0005-1098(76)90076-5.

[39] Saetti, U., Enciu, J., and Horn, J. F., "Flight Dynamics and Control of an eVTOL Concept Aircraft with a Propeller-Driven Rotor,"

Journal of the American Helicopter Society, **67**, 032012 (2022), doi: https://doi.org/10.4050/JAHS.67.032012.

[40] Saetti, U., and Horn, J. F., "Implementation and Linearization of State-Space Free-Vortex Wake Models for Rotary- and Flapping-Wing Vehicles," *Journal of the American Helicopter Society*, **68**, 042004 (2023), doi: https://doi.org/10.4050/JAHS.68.042004.

[41] Saetti, U., Rogers, J. D., Alam, M., and Jump, M., "Tau Theory-Based Flare Control in Autonomous Helicopter Autorotation," *Aerospace*, **11**, 33(2024), doi: https://doi.org/10.3390/aerospace11010033.

[42] Saetti, U., Horn, J. F., and Berger, T., "On the Effects of Rotor Induced Vibrational Stability on Helicopter Flight Dynamics," *CEAS Aeronautical Journal,* Vol. 15, 2024, pp. 439–458, doi: https://doi.org/10.1007/s13272-024-00718-w.

[43] Saetti, U., "Dynamic Inversion Flight Control Laws for Autonomous Transition of Tilt-Rotor Aircraft," Proceedings of the Second International Conference on Advanced Air Mobility Systems (ICAAMS-2), Singapore, December 4–5, 2024.

[44] Berger, T., Tischler, M. B., and Horn, J. F., "High-Speed Rotorcraft Pitch Axis Response Type Investigation," Proceedings of the 77th Annual Forum of the Vertical Flight Society, Virtual, May 10–14, 2021, doi: https://doi.org/10.4050/F-0077-2021-16793.

[45] Sahani, N. A., and Horn, J. F., "Adaptive Model Inversion Control of a Helicopter with Structural Load Limiting," *Journal of Guidance, Control, and Dynamics*, Vol. 29, (2), 2006, pp. 411–420, doi: https://doi.org/10.2514/1.13391.

[46] Theron, J. P., Horn, J. F., Wachspress, D. A., and Enciu, J., "Nonlinear Dynamic Inversion Control for Urban Air Mobility Aircraft with Distributed Electric Propulsion," Proceedings of the 76th Annual Forum of the Vertical Flight Society, October 5–8, 2020, doi: https://doi.org/10.4050/F-0076-2020-16396.

[47] Walter, A., McKay, M., Niemiec, R., Gandhi, F., and Berger, T., "Hover Dynamics and Flight Control of a UAM-Scale Quadcopter with Hybrid RPM and Collective Pitch Control," *Journal of the American Helicopter Society*, **68**, 022012 (2023), doi: https://doi.org/10.4050/JAHS.68.022012.

[48] Enciu, J., Horn, J. F., and Langelaan, J. W., "Formation Control of a Rotorcraft Multilift System," *Journal of the American Helicopter Society*, **62**, 042011 (2022), doi: https://doi.org/10.4050/JAHS.62.042011.

[49] Spires, J. M., and Horn, J. F., "Multi-Input Multi-Output Model-Following Control Design Methods for Rotorcraft," *Journal of the American Helicopter Society*, **66**, 032002 (2021), doi: https://doi.org/10.4050/JAHS.66.032002.

[50] Scaramal, M., and Horn, J. F., "Load Alleviation on Compound Rotorcraft Using Load Feedback and Extremum Seeking Control," *Journal of Guidance, Control, and Dynamics*, Vol. 46, (12), 2023, 2399–2408, doi: https://doi.org/10.2514/1.G007192.

[51] Ivler, C., and Juhansz, O., "Evaluation of Control Allocation Techniques for a Medium Lift Tilt-Rotor," Proceedings of the 71st Annual Forum of the American Helicopter Society, Virginia Beach, VA, May 5–7, 2015.

[52] Saetti, U., Horn, J. F., Berger, T., and Tischler, M. B., "Handling-Qualities Perspective on Rotorcraft Load Alleviation Control," *Journal of Guidance, Control, and Dynamics*, 2020, pp. 1–13, doi: https://doi.org/10.2514/1.G004965.

[53] Saetti, U., "Dynamic Inversion Flight Control Laws for Autonomous Transition of Tilt-Rotor/Wing Aircraft," *Journal of the American Helicopter Society*, **70**, 032005 (2025), doi: https://doi.org/10.4050/JAHS.70.032005.

[54] Blakelock, J. H., *Automatic Control of Aircraft and Missiles*, John Wiley & Sons, New York, NY, 1965, doi: https://doi.org/10.1017/S0001924000057912.

[55] Tischler, M. B., Berger, T., Ivler, C. M., Mansur, M. H., Cheung, K. K., and Soong, J. Y., *Practical Methods for Aircraft and Rotorcraft Flight Control Design: An Optimization-Based Approach*, American Institute of Aeronautics and Astronautics, Reston, VA, 2017.

[56] Anon, "Handling Qualities for Military Rotorcraft," Technical Report, Department of Defense, IL-DTL-32742, Redstone Arsenal, AL, 2023.

[57] Berger, T., Ivler, C. M., Berrios, M. G., Tischler, M. B., and Miller, D. G., "Disturbance Rejection Handling Qualities Criteria for Rotorcraft," Proceedings of the 72nd Annual Forum of the Vertical Flight Society, West Palm Beach, FL, May 16–19, 2016.